Level structure of ^{21}Mg: Nuclear and astrophysical implications

A. St. J. Murphy,* M. Aliotta, T. Davinson, C. Ruiz,† and P. J. Woods
School of Physics, University of Edinburgh, Mayfield Road, Edinburgh, EH9 3JZ, United Kingdom

J. M. D'Auria
Simon Fraser University, Burnaby, British Columbia V5A 1S6, Canada

L. Buchmann, A. A. Chen,‡ A. M. Laird,§ F. Sarazin,‖ and P. Walden
TRIUMF, Vancouver, British Columbia V6T 2A3, Canada

B. R. Fulton and J. E. Pearson†
University of York, York, YO10 5DD, United Kingdom

B. A. Brown
National Superconducting Cyclotron Facility, Michigan State University, East Lansing, Michigan 48824, USA
(Received 30 November 2005; published 28 March 2006)

Resonant elastic scattering of a radioactive ^{20}Na beam incident upon protons in a polyethylene target has been used to probe the level structure of ^{21}Mg above the proton decay threshold. Three states have been observed, and their properties deduced through analysis based on the *R*-matrix formalism. The results improve and extend previous studies of this nucleus. An estimate of the ^{20}Na$(p,\gamma)^{21}$Mg reaction rate, including these new data, suggests this reaction will not play a significant role in explosive hydrogen burning in astrophysical sites such as novae and x-ray bursts.

DOI: 10.1103/PhysRevC.73.034320 PACS number(s): 21.10.−k, 26.30.+k, 26.50.+x, 27.30.+t

I. INTRODUCTION

Little is known about the level structure of the radionuclide ^{21}Mg or, indeed, of any of the other $T_z = -\frac{3}{2}$ *sd*-shell nuclei. Therefore, even at relatively low excitation energies, new data provide important tests of nuclear models and shell structure in this region. Moreover, these nuclei may lie along the path of nucleosynthesis that occurs in accretion-driven explosive hydrogen burning, as is thought to occur in evolved binary systems such as novae and x-ray bursters. It is the energy released by the nuclear reactions that drives these explosions; thus, a vital ingredient in modeling these phenomena is knowing the nuclear reaction rates involved. The reaction pathways involve resonant proton- and α-capture reactions (as well as β decays), but the intrinsic cross sections are small, making direct measurements of these rates difficult. Since these rates are dominated by resonant processes, an alternative approach is to calculate the reaction rate using detailed knowledge of the nuclear states involved.

The exotic nature of these nuclei means that accessing them is extremely difficult. Previously, β-decay studies as well as multinucleon transfer reactions were employed to study $A = 21$, $T = \frac{3}{2}$ states [1–3]. The relevance of the former technique is limited because of the very different selectivity, while the latter technique has the additional problem of highly model-dependent extraction of nuclear parameters. Newly available, intense, low energy radioactive beams mean that the technique of resonant elastic scattering may now also be used as a probe of these nuclei. This approach has several advantages. First, it naturally lends itself to the study of astrophysically important states just above the proton threshold in the compound nucleus being populated. Second, the nuclear and Coulomb interaction is such that resonant effects readily appear in the excitation function. Finally, while resonant scattering data are also subject to model-dependent analysis, the uncertainties are significantly smaller.

Here, we have employed resonant elastic scattering in inverse kinematics to determine energies, spins, and widths of states above the proton threshold at 3.226 MeV [4] in ^{21}Mg.

II. EXPERIMENTAL DETAILS

The experiment was performed using the TRIUMF–UK detector array (TUDA) at TRIUMF and was similar to that employed in the measurement of the ^{21}Na$(p,p)^{21}$Na reaction [5,6]. The isotope separator accelerator facility (ISAC-I) [7] employed a driver beam of $\sim$20 μA of 500 MeV protons incident upon a primary silicon carbide target. ^{20}Na^{5+} ions were extracted and accelerated to 1.250 and 1.600 MeV/u. The beam was bunched and delivered in pulses separated by 86 ns.

*Electronc address: a.s.murphy@ed.ac.uk
†Present address: TRIUMF, Vancouver, BC V6T 2A3, Canada.
‡Present address: McMaster University, Hamilton, ON L8S 4M1, Canada.
§Present address: University of York, York, YO10 5DD, UK.
‖Present address: Colorado School of Mines, Golden, CO 80401, USA.

The beam energy was determined using both the calibrated ISAC-I Prague magnet, and using the DRAGON spectrometer [8]. The latter involved focusing the beam onto slits after the first magnetic dipole and measuring the independently calibrated field. For the higher beam energy, when the field of the DRAGON MD1 magnet was insufficient to bend the beam, this required first introducing gas into the DRAGON target volume to slow the ions. Measurements of the required magnetic fields were performed with various pressures of gas, and an extrapolation to zero gas pressure made. The measurements of the beam energy with the Prague magnet and with DRAGON agreed to better than $\sim$1 keV/u.

The post-accelerated ions were then directed upon an experimental target of $(CH_2)_n$, provided by the Centre de Recherches du Cyclotron, Louvain-la-Neuve. This had a thickness of $\sim$795 μg/cm^2 ($\pm$10%) determined by weighing the targets and was consistent with energy loss incurred by ions detected after traversing the target. Typical ^{20}Na beam intensities of a few *epA* were measured at the secondary target. Elastically scattered proton recoils were detected in 300 μm thick MSL type YY1 silicon strip detectors [9] as used with the Louvain-Edinburgh detector array (LEDA). Since the heavy-ion projectile loses a significant fraction of its energy in passing through such a thick target, elastic scattering reactions occurring at different depths correspond to a wide range of center-of-mass (c.m.) energies. The proton energy spectrum observed by a detector element at a given angle may then be interpreted as an excitation function. This experimental configuration therefore permits simultaneous excitation functions and angular distributions to be collected. Several incident beam energies may be used to further extend the excitation function coverage. For these measurements, data were collected at two beam energies corresponding to 0.51–1.20 MeV in the center of mass for the lower energy and to 0.91–1.54 MeV for the higher beam energy.

A schematic diagram of the experimental setup is shown in Fig. 1. Two LEDAs were placed 19.5 and 60.5 cm downstream of the target, covering laboratory angles of 14.4°–33.7° and 4.7°–12.1°, respectively. A complete LEDA consisting of eight identical sectors, segmented into 16 annular elements, was used for the most downstream detector; while four sectors in a "cross" configuration were used for the detector that was nearer the target. The polar angular resolution achieved was thus about 1.2° for the near-to-target detector and 0.45° for the far detector. To protect the detectors from radiation damage induced by the high flux of elastically scattered beam particles, thin Mylar sheeting was positioned $\sim$0.6 cm in front of each detector. The thicknesses of these foils was chosen so as to just stop the highest energy ^{20}Na ions elastically scattered from either of the target atom species, and thus was thinner for the nearer detector that observed wider angles. When the beam energy was adjusted, the Mylar protective foils were changed appropriately. The thicknesses of the Mylar protective foils were determined using an α-particle source. The energy loss incurred by protons exiting the target and passing through the Mylar sheeting and detector dead layer, although small, was corrected for in all data analyzed. One sector on the near-to-target detector was left unshielded to provide online diagnostics.

The radioactive beam intensity was monitored and recorded using a high sensitivity, electrically suppressed Faraday cup. The beam intensity could also be determined from comparison of the yield of elastically scattered protons, measured in a region with no resonance effect, to the yield expected from the Rutherford formula. This information was used for the absolute normalization and found to agree with a subsequent analysis to typically better than 5%. Similarly, the symmetry of these events with respect to scattering angle was monitored so as to confirm an accurate target-LEDA alignment.

A high precision pulser was used to determine analog-to-digital converter offsets and linearities, while the response of each LEDA was calibrated through use of a standard triple-α source containing the isotopes ^{239}Pu, ^{241}Am, and ^{244}Cm. The typical resolution of the α peak at 5.486 MeV was 31 keV full width at half maximum (FWHM) for a single detector element. Purely electronic noise, as measured with the pulser, contributed around 18 keV FWHM. In a subsequent analysis of proton events, the energy calibration was modified to include the well-known pulse height defect for α particles relative to protons [10].

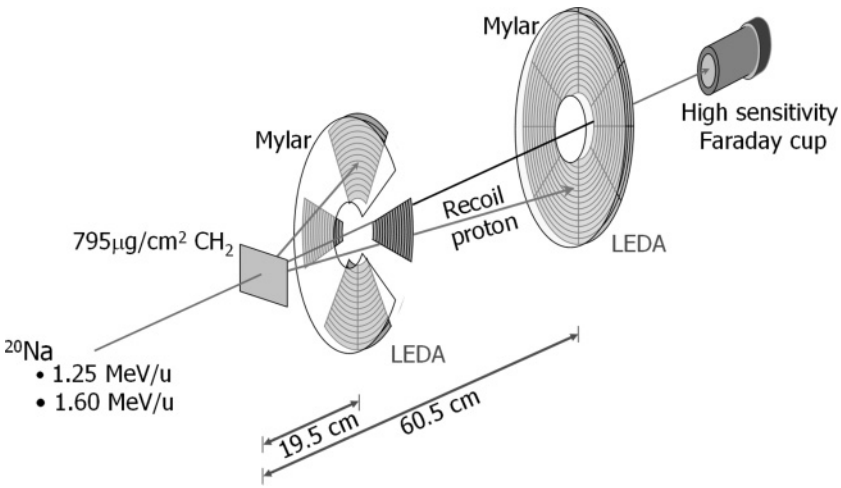

FIG. 1. Schematic diagram of the experimental apparatus employed at the TUDA facility.

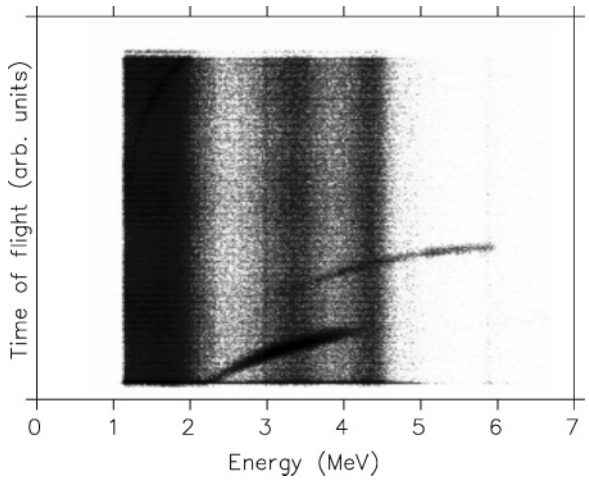

FIG. 2. Plot of laboratory energy vs TOF for all particles detected at 5.3° for the 1.600 MeV/u beam energy data set. Broad vertical bands correspond to α particles originating from the decay of ^{20}Na beam ions stopped near the detectors; curved loci are elastically scattered protons (upper locus) and carbon ions (lower locus).

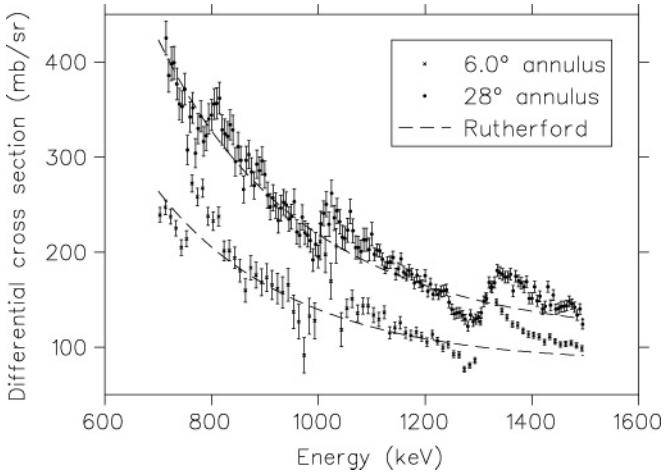

FIG. 3. Differential cross sections for protons detected in two summed annuli around 6° and one annulus around 28° (lab), as a function of their c.m. energy. Data taken at both the 1.250 and 1.600 MeV/u beam energies are included. Dashed lines are the pure Coulomb scattering expectations. Error bars assume Poissonian statistical effects only.

Figure 2 shows a plot of the energy of detected particles (in the laboratory frame) versus time of flight (TOF) for all data taken at the 1.600 MeV/u beam energy setting and scattered into the annulus of detector elements located at a polar angle of 5.3°. The vertical bands are caused by β-delayed α-particle decay of ^{20}Na ions that stopped in the protective Mylar sheets. The more penetrating β particles contribute an intense band at low energies, whereas α particles are responsible for the multiple higher energy bands. Depending on the random orientation with which the α decay occurs, the α particles can pass through various thicknesses of Mylar before entering the detectors, leading to severe broadening of these lines. Elastic scattering of the ^{20}Na beam from carbon atoms in the target occurs at a relatively high c.m. energy, resulting in some recoiling carbon ions having sufficient energy to escape the Mylar foils. These events are seen as the lower of the curved loci in Fig. 2. The final well-separated locus corresponds to the events of interest: elastically scattered protons.

The data acquisition was operated such that the time-to-digital converter (TDC) started at the detection of a particle and stopped at the next accelerator rf signal. Thus, faster moving ions have larger TDC conversions. Additionally, the use of leading-edge discriminators in the timing of the start signal means that signals of larger amplitude start earlier. These combined effects lead to the observed shape of the locus. A suitable algorithm applied to the TDC signal allows these effects to be removed and thus the proton locus linearized. A simple software cut may then be implemented to select the region corresponding to the elastically scattered protons, as well as nearby regions which determine the α-decay background. These may be subtracted from one another, normalized to the experimental conditions, and projected as c.m. energy against differential cross section. Figure 3 shows such spectra for protons detected toward the extremes of the angular range covered and reveals the existence of three resonances at c.m. energies close to 780, 1000, and 1320 keV. These persist over the angular range covered. At some energies, the α-decay background was strong (up to twice the intensity of the proton signal), and consequently larger error bars are seen for those data points. Also shown in Fig. 3 for comparison is the Coulomb scattering cross section.

The experimental resolution for these data has several contributions: the intrinsic energy resolution of the detectors, straggling effects as particles traverse the target and pass through the protective Mylar sheets and detector dead layer, and the finite opening angles subtended by silicon elements. An effective method for estimating the resulting overall energy resolution has been developed [11] and entails fitting a Gaussian to the highest energy data corresponding to the target's upstream surface. For data from the LEDA located at 60.5 cm from the target, a value for the experimental energy resolution of 7.0 keV (c.m.) was found. This is reasonable in light of the study of Ruiz *et al.* [6] which used similar beam species and energies but thinner targets (250 μg/cm^2) and found an experimental energy resolution of 5 keV (c.m.). This is a free parameter in the fitting of the data used to extract resonance properties (see Sec. III), and thus the dependence of the quality of the fit as a function of this parameter may be considered. For a typical final fit, the overall χ^2 per degree of freedom as a function of the experimental resolution is shown in Fig. 4; the minimum is in excellent agreement with the value of 7 keV.

Unfortunately, as has been the case for experiments with a nearly identical configuration [5,6], the data collected in the near-to-target LEDA have proven to be harder to analyze. The reason for this appears to be related to the rapidly increasing energy losses and straggling incurred by events scattered to the large angles. For this reason, these data have not been included in the subsequent analysis, although they are of significant use in illustrating the overall trend in the data.

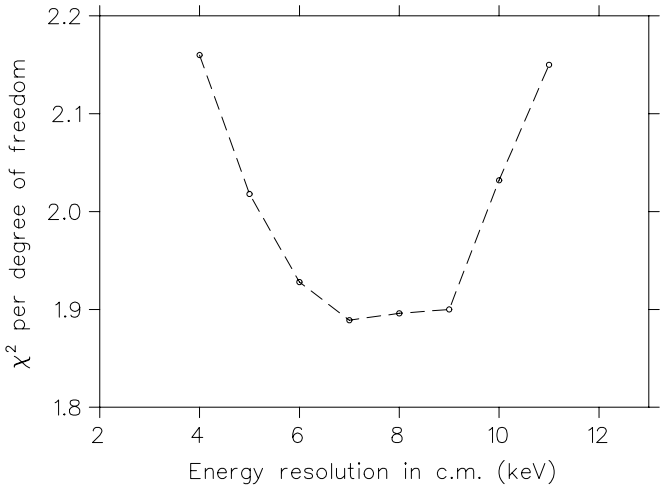

FIG. 4. Dependence of the quality of fit parameter χ^2 for an *R*-matrix fit to the data (fit 1 in Table I) as a function of the assumed experimental energy resolution. While the quality of fit drops significantly away from the expected value of 7 keV, the extracted energy and width parameters show little sensitivity. The dashed line is to guide the eye.

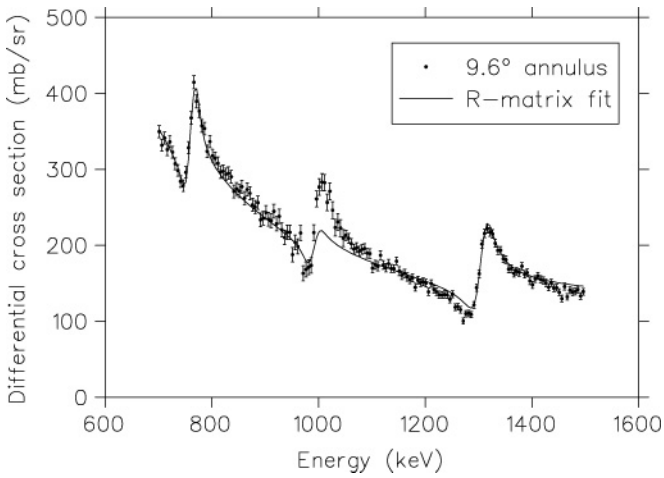

FIG. 5. Differential cross section against c.m. energy for protons scattered to 9.6° in the ^{20}Na$(p,p)^{20}$Na reaction. The curve shows an *R*-matrix fit to the data assuming the three resonances are proceeding through states of spin $J = \frac{3}{2}$ in ^{21}Mg, with the lowest and highest resonances populated by *s*-wave protons, while the middle resonance has *p*-wave character. The good quality of fit in the region where *s*-wave population is assumed is a common feature of all three resonances, as is the poor quality of the fit in the region where *p*-wave population is assumed.

III. RESULTS AND *R*-MATRIX ANALYSIS

The data accrued have been analyzed within the *R*-matrix formalism [12,13], using the data analysis package of Ruiz *et al*. [6], modified slightly to allow inclusion of states of half-integer spin. Because of the difficulties encountered with accurately calibrating the near-to-target detector, subsequent *R*-matrix analysis includes simultaneous fits to data consisting of protons collected with energies between 700 and 1500 keV (c.m.) at 13 angles between 4.8° and 10.3° (lab).

The methodology of the *R*-matrix approach is detailed in [6] but may be summarized as follows. One initially makes an assumption for the angular momentum transfer involved and for the spins of the states in the compound nucleus through which each resonance is being populated. The scattering cross section is then calculated for all energies and angles at which data exist, based on initial estimates for the *R*-matrix pole energies and widths of the states. These cross sections are compared with experimental data. Parameters are then varied iteratively until the minimum in the quality of fit parameter, χ^2, is found. One may then make quantitative comparisons between alternative possibilities for the angular momentum transfer and spins of the states in the compound nucleus that may be involved. The values for the pole energies and widths of the states involved, as determined by the optimal fit to the data, may then be converted to real observable parameters through use of the boundary transformation [14].

Following this procedure for the present data set, one finds that all three of the resonant structures are well fitted as *s*-wave resonances, whereas there is an inability to obtain a good fit involving nonzero angular momentum transfers. To illustrate this, Fig. 5 shows a comparison between the measured proton differential cross section at 9.6° and a global fit to the data assuming that the structure near proton energies of 1000 keV (lab) is a *p*-wave resonance; while the remaining two resonances are of *s*-wave character. The fit to the data is clearly much better for the upper and lower, *s*-wave assumed resonances, while the fit to the middle resonance, where *p*-wave angular momentum transfer has been assumed, is poor. This behavior is common to all three resonances seen; they are all well descibed by *s* waves and poorly described by any other angular momentum transfer.

The ground state of ^{20}Na is known to have a spin-parity of 2^+; therefore, given that the three features observed are all *s*-wave resonances, the states being probed in ^{21}Mg must have either $J = \frac{3}{2}$ or $J = \frac{5}{2}$, depending on the alignment of the proton's spin. Since states of the same spin will interfere, each of the eight possible combinations for the spins of these three states must be evaluated separately. In principle, the quality of an *R*-matrix fit to the data for each of these possibilities can provide discrimination between them. Table I lists the minimum χ^2 per degree of freedom obtained in each case, together with the properties of the states in ^{21}Mg that these fits suggest. Although it is the formal *R*-matrix pole parameters that are being fitted to the data, here we have applied the boundary transformation method of Barker [6,14] so that the energies and widths quoted are "observable" parameters, easing comparisons with past and future data. The accuracy with which the energy and width parameters can be extracted has been evaluated by performing additional fits in which input parameters were modified by their experimental uncertainty. The uncertainty in the energies of the resonances is dominated by the uncertainty in the absolute scattering angle ($\sim$0.2°), with similar additional contributions from the statistical quality of fit to the data and the uncertainty on the thickness of the protective Mylar foils. The uncertainty

TABLE I. Energy, proton decay widths, and reduced widths for states in ^{21}Mg, obtained through *R*-matrix analysis, for each of the possible combinations of spins for the states.

Fit	χ^2/N	Resonance 1				Resonance 2				Resonance 3			
		J	E^{a} (keV)	Γ_p (keV)	γ_c (MeV$^{1/2}$)	J	E^{b} (keV)	Γ_p (keV)	γ_c (MeV$^{1/2}$)	J	E^{c} (keV)	Γ_p (keV)	γ_c (MeV$^{1/2}$)
1	1.90	$\frac{3}{2}$	779	8 ± 3	0.81	$\frac{3}{2}$	1004	5^{+4}_{-2}	0.31	$\frac{3}{2}$	1312	42 ± 8	0.53
2	2.50	$\frac{3}{2}$	779	8 ± 3	0.82	$\frac{3}{2}$	1000	10 ± 3	0.44	$\frac{5}{2}$	1311	12 ± 4	0.27
3	2.38	$\frac{3}{2}$	780	8 ± 3	−0.85	$\frac{5}{2}$	1002	5^{+4}_{-2}	−0.31	$\frac{5}{2}$	1310	12 ± 4	0.27
4	2.32	$\frac{5}{2}$	770	4^{+4}_{-2}	−0.58	$\frac{5}{2}$	1001	4^{+4}_{-2}	0.29	$\frac{5}{2}$	1309	17 ± 5	0.33
5	1.95	$\frac{3}{2}$	780	8 ± 3	0.86	$\frac{5}{2}$	1002	5^{+4}_{-2}	0.29	$\frac{3}{2}$	1312	65 ± 8	0.69
6	2.29	$\frac{5}{2}$	769	4^{+4}_{-2}	0.55	$\frac{5}{2}$	1001	4^{+4}_{-2}	0.29	$\frac{3}{2}$	1313	23 ± 5	0.38
7	2.36	$\frac{5}{2}$	770	4^{+4}_{-2}	0.60	$\frac{3}{2}$	1004	8 ± 3	0.40	$\frac{5}{2}$	1309	22 ± 5	0.38
8	2.09	$\frac{5}{2}$	769	4^{+4}_{-2}	0.56	$\frac{3}{2}$	1005	9 ± 3	−0.41	$\frac{3}{2}$	1312	24 ± 6	0.38

[a] ±6 keV.
[b] ±5 keV.
[c] ±5 keV.

in the width is dominated by the quality of the fit, with an additional contribution from the uncertainty in the experimental energy resolution (especially for small widths).

The channel radius, which is the boundary between the internal and external regions of the nuclear potential, was chosen to be close to the physical radius of the ^{20}Na+p system. In these calculations, a value of 4.5 fm was chosen based on the empirical formula $r = 1.2(A_1^{1/3} + A_2^{1/3})$. The dependence of the *R*-matrix formalism upon this parameter was investigated, and a shallow minimum close to 4.5 fm found. Similarly, the dependence of the fitting procedure upon binning width, both with respect to energy and angle, has been studied. No significant effects have been observed for reasonable alternative choices. This is expected, since the width of the energy bins is close to the intrinsic experimental resolution, and the angular dependence is smooth. Likewise, it is known that the *R*-matrix formalism is independent of the boundary condition; this has been confirmed for the present analysis.

An example of global fit, showing simultaneous fits to the entire data set, is shown in Fig. 6. The two best global fits occur when the data are fitted assuming the upper and lower resonances correspond to states in ^{21}Mg that have spin $J = \frac{3}{2}$. There is little discrimination between the two possibilities for the spin of the middle resonance. When any attempt is made to fit the upper resonance as a $J = \frac{5}{2}$ state, significantly poorer fits are obtained.

If the lowest resonance corresponds to a $J = \frac{3}{2}$ state in ^{21}Mg, then it appears to be located at an energy $E_r = 779$ keV [$E_x(^{21}\text{Mg}) = 4.005$ MeV], and has a width of ∼8 keV. Alternatively, if it is a $J = \frac{5}{2}$ state, it appears to be located at $E_r = 770$ keV [$E_x(^{21}\text{Mg}) = 3.996$ MeV] and has a width of ∼4 keV. The middle resonance, located at $E_r = 1002$ keV [$E_x(^{21}\text{Mg}) = 4.228$ MeV], has a width of either ∼4.5 ($J = \frac{3}{2}$) or 9 keV ($J = \frac{5}{2}$). The *R*-matrix analysis provides little discrimination between the possible spin combinations for these two states, except for a slight preference for them both being $J = \frac{3}{2}$ and rejection of them both being $J = \frac{5}{2}$.

To attempt to confirm the precise nature of the states in ^{21}Mg at ∼4.000 and 4.228 MeV, additional comparisons must be made.

IV. ANALOG STATES AND SHELL MODEL CALCULATIONS

Current knowledge of ^{21}Mg and its isobaric analog ^{21}F in the excitation energy region around 4.0–4.5 MeV is extremely limited. For ^{21}Mg, the only relevant data come from the study of the ^{24}Mg(^{3}He,^{6}He)^{21}Mg reaction by Kubono *et al.* [3]. Several states were observed, and tentative spin assignments for some of the states were made on the basis of distorted-wave Born approximation fits to angular distributions. No width information was obtained. Spectroscopic information on ^{21}F comes principally from two sources: von Neumann-Cosel [1] and Alburger [2]. In the region of interest, there are several states: but once again, spin assignments, where made, are only tentative, and no width information exists.

Further progress in identifying the nature of the states seen may be made in two ways. First, one can take advantage of isospin symmetry and make comparisons to known $T = \frac{3}{2}$ states in the neighboring $T_z = \frac{1}{2}$ nuclei, ^{21}Ne and ^{21}Na [4]. These data (with energies adjusted such that the lowest $T = \frac{3}{2}$ states match the ground states in the $T_z = \frac{3}{2}$ nuclei) are shown together with the current knowledge of the level schemes of ^{21}Mg and ^{21}F [4] in Fig. 7. Due to its stability, the accumulated spectroscopic knowledge of ^{21}Ne is such that this can provide significant extra information. Secondly, a shell model calculation for the $A = 21$ system may be performed. We used the OXBASH code [15], employing the Wildenthal USD interaction [16] in the *sd*-shell model space. Only positive parity states are calculated. Table II lists the calculated excitation energies and spectroscopic factors for $0s1/2$ states that appear to be possible matches to those seen in the present work, while all the calculated states are shown in Fig. 7, together with the present experimental data.

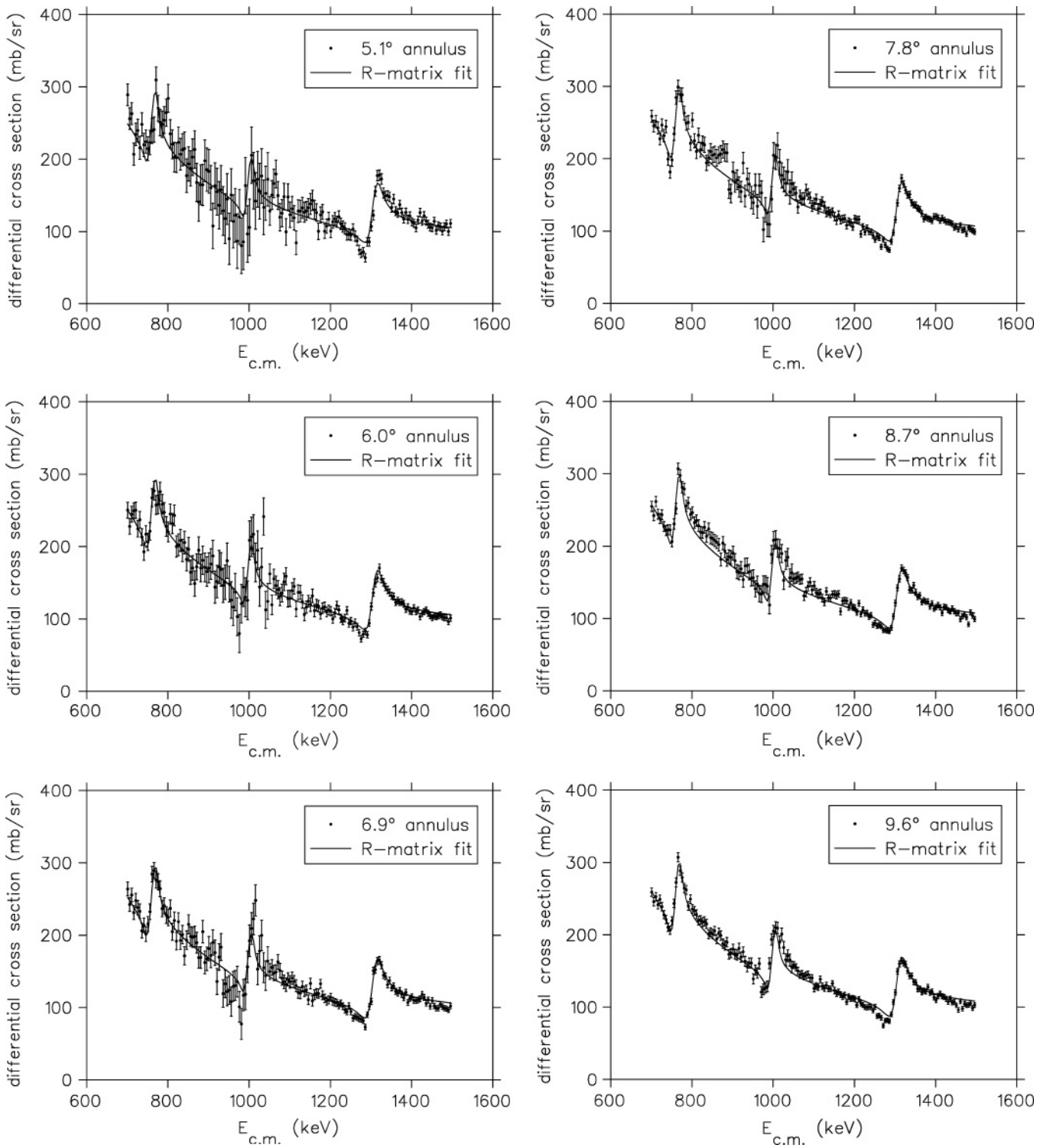

FIG. 6. Global R-matrix fit (fit 5 in Table I), assuming all resonances are of s-wave character and correspond to states in ^{21}Mg which have, in ascending energy, $J = \frac{3}{2}$, $\frac{5}{2}$, and $\frac{3}{2}$. Pairs of LEDA annuli have been summed to improve statistics.

Taken together, the comparisons that may be made using Fig. 7 are quite revealing. The ground state and first excited state (or its $T = \frac{3}{2}$ analog) are identified in all level schemes. At just over 1 MeV, a negative parity state, probably $J^\pi = \frac{1}{2}^-$, is seen in ^{21}F, ^{21}Ne, and ^{21}Mg. The shell model predicts a doublet consisting of a $J^\pi = \frac{3}{2}^+$ and a $\frac{9}{2}^+$ state at about 1.85 MeV, and there is clear evidence of these states in the ^{21}F and ^{21}Ne level schemes, lowered in energy by about 100 keV. The next positive parity states predicted are a cluster of four states ($J^\pi = \frac{3}{2}^+$, $\frac{7}{2}^+$, $\frac{5}{2}^+$, and $\frac{9}{2}^+$) between 3.5 and 3.7 MeV

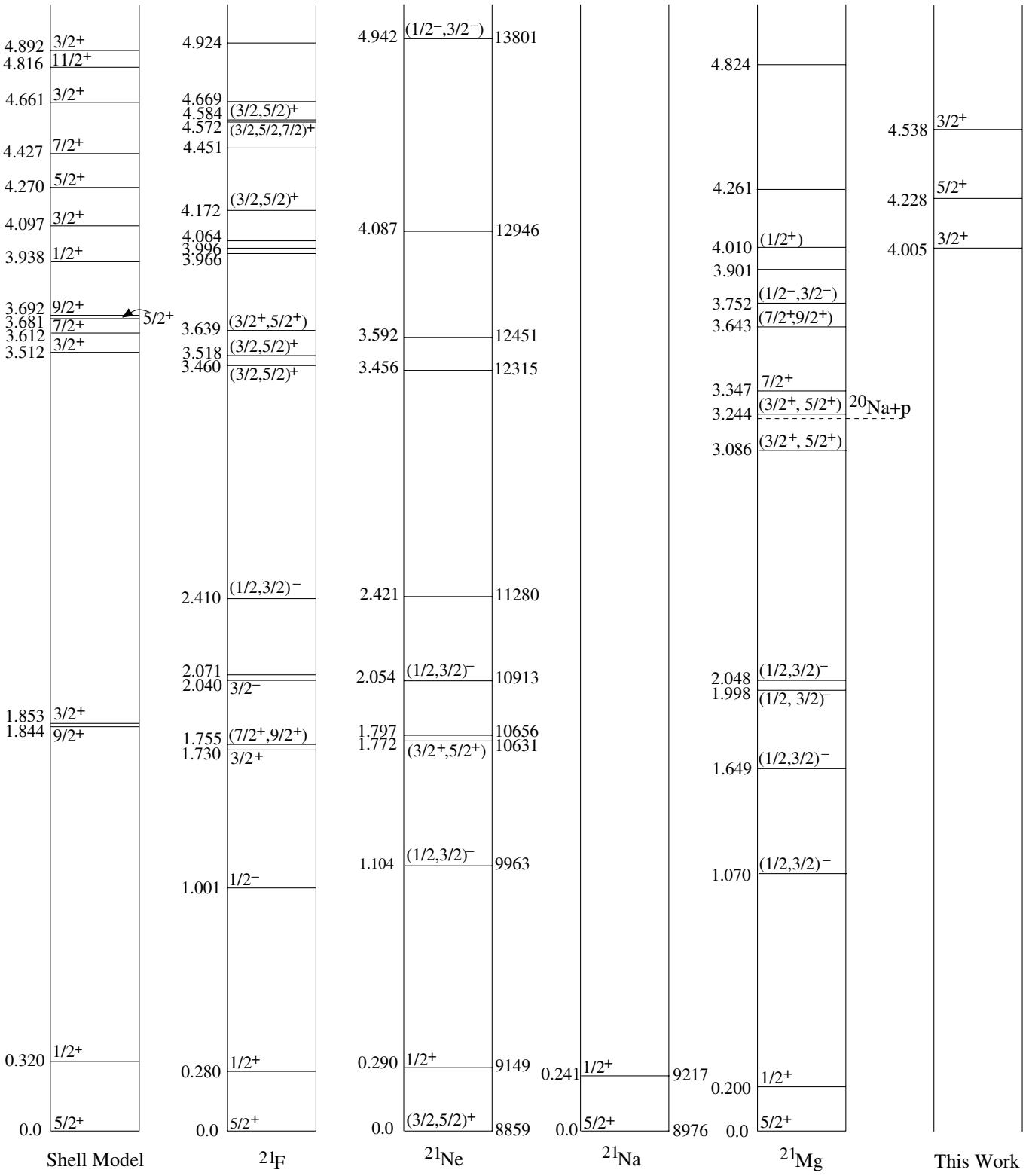

FIG. 7. Level schemes for $A = 21$ nuclei. Spins and parities of states are shown where known, brackets indicating the assignment is tentative. Numbers to the left of level schemes are excitation energies, except in the cases of ^{21}Ne and ^{21}Na where the difference between the level and the lowest $T = \frac{3}{2}$ state is shown. In these cases, the excitation energy is shown to the right of the level scheme. The dashed line is the proton threshold in ^{21}Mg at 3.226 MeV.

TABLE II. OXBASH shell model prediction of the $0s1/2$ states in $T = \frac{3}{2}$, $A = 21$, using the USD interaction.

J	n	E	C^2S
$\frac{3}{2}$	3	4.097	0.082
$\frac{5}{2}$	3	4.270	0.279
$\frac{3}{2}$	4	4.661	0.238
$\frac{3}{2}$	5	4.892	0.329
$\frac{5}{2}$	4	5.123	0.057

excitation. Three candidate states have been discovered in ^{21}F at about these energies, and similarly three candidate states are seen in ^{21}Mg a few hundred keV lower. The reduced excitation energies for more proton-rich nuclei are consistent with the well-known Coulomb level shift [12,13]. Two states, presently with no spin assignment, are seen at these energies in ^{21}Ne and could be analogs to these states.

The next positive parity level predicted by the shell model has a $J^\pi = \frac{1}{2}^+$ and is located at 3.938 MeV. This could be the $(\frac{1}{2}^+)$ state that was thought to have been seen in the work of Kubono *et al.* [3] at 4.010 MeV; but if this were, so one might have expected it to be visible in the present work (although the penetrability for $\ell = 2$ transitions makes the sensitivity of the present experiment to $J^\pi = \frac{1}{2}^+$ states low). Moreover, the level shifts observed for other states result in a reduction of excitation energy for states in ^{21}Mg as compared to ^{21}F or the shell model, whereas this would require a small upward shift. There are several other known states in ^{21}Mg, for example, the state of unknown assignment at 3.901 MeV, and these are more likely candidates for the $J^\pi = \frac{1}{2}^+$ state.

At 4.097 MeV in the shell model calculation, a $J^\pi = \frac{3}{2}^+$ state is predicted, followed by a $J^\pi = \frac{5}{2}^+$ state at an excitation of 4.270 MeV. In the present work, strong resonances were observed corresponding to ^{21}Mg excitation energies of $\sim$4.000 and 4.228 MeV, for which the R-matrix analysis was unable to distinguish between possible $J^\pi = \frac{3}{2}^+$ or $J^\pi = \frac{5}{2}^+$ assignments (although it did suggest the two states would not both have $J^\pi = \frac{5}{2}^+$). Given that the $J^\pi = \frac{5}{2}^+$ state is expected at higher energy, that there are no other $J^\pi = \frac{5}{2}^+$ states nearby, and the reasonable level shifts implied, it seems likely that the higher of these two observed states is indeed $J^\pi = \frac{5}{2}^+$ and the lower is $J^\pi = \frac{3}{2}^+$.

One may also compare the observed widths of the states with the prediction of the shell model. This is determined by the product of the calculated spectroscopic factor, C^2S (see Table II) and the full single-particle proton widths. These were calculated from the proton scattering cross section with a Woods-Saxon potential. The $\ell = 0$ peak energy was varied by changing the well depth of the potential in order to find the full width at half maximum as a function of proton-decay Q value. Figure 8 shows the predicted single-particle proton width for s-wave protons in ^{21}Mg as a function of resonance energy. The resulting shell model prediction for the width of these states is $\sim$2 keV for the state at 4.005 keV and $\sim$16 keV for the state at 4.228 keV. This prediction compares with the observed

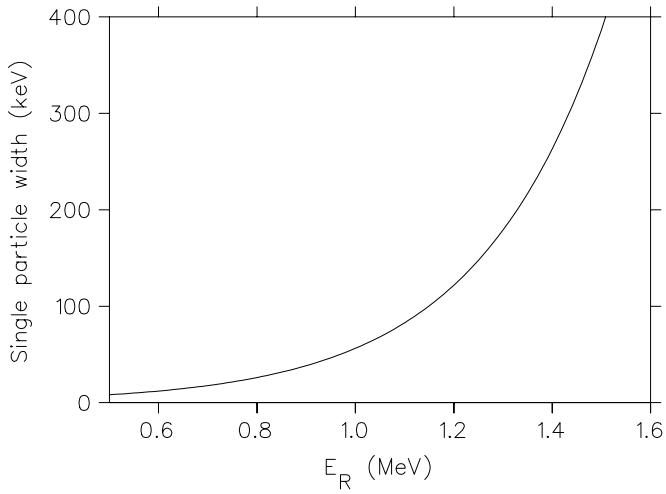

FIG. 8. Single-particle width Γ_{sp} as a function of resonance energy for $\ell = 0$ states in ^{21}Mg.

widths of 8 ± 3 and 4^{+4}_{-2} keV, respectively. This suggests that the spectroscopic factors for the $J^\pi = \frac{3}{2}^+$ state may in fact be somewhat larger than predicted; and for the $J^\pi = \frac{5}{2}^+$ state, somewhat smaller.

In light of these arguments, it appears that the state seen at 4.010 ± 0.015 MeV in the work of Kubono *et al.* [3], and tentatively assigned $J^\pi = \frac{1}{2}^+$, should in fact have been identified as $J^\pi = \frac{3}{2}^+$. The state seen in ^{21}Ne at 4.087 MeV, currently with no assignment, has an excitation that suggests it may well be the analog to this state. In the data of Kubono *et al.*, a state at $E_x = 4.261$ MeV was observed, but that work was unable to identify the angular momentum transfer involved. This might be the $J^\pi = \frac{5}{2}^+$ state seen at 4.228 MeV in the present data, although the discrepancy in the two energies seems to be more than the uncertainties permit.

At 4.427 MeV, the shell model predicts a $J^\pi = \frac{7}{2}^+$ state. No candidate state is seen in the present data, but this may simply be due to the low angular momentum available in the entrance channel. The final state observed in the present data, at an energy of 4.538 MeV, was confidently assigned $J^\pi = \frac{3}{2}^+$ on the basis of the R-matrix analysis. This very likely corresponds to the state predicted by the shell model calculation at 4.661 MeV, the implied level shift being consistent with others in the region. The partial width of this state is observed to be 65 keV. This compares well with the spectroscopic factor (C^2S) of 0.238 predicted by the shell model, which, including the penetrability factor appropriate for the excitation, results in a predicted width of 45 keV.

It might seem surprising that there appears to be no state in the Kubono *et al.* data set that could be a match to the state at $E_x = 4.538$ MeV seen here. However, in those data a strong background signal due to a ^{12}C target contaminant was present between excitation energies of 4.3 and 4.8 MeV.

V. ASTROPHYSICAL IMPLICATIONS

In the original conception of the rp-process [17], breakout from the hot CNO cycle was thought to occur via

TABLE III. Parameters used in calculating the ^{20}Na(p,γ)^{21}Mg astrophysical reaction rate.

E_x (^{21}Mg) (MeV)	E_r (keV)	J^π	Γ_p (MeV)	Γ_γ (MeV)	$\omega\gamma$ (eV)
3.244[a]	28	$\frac{5}{2}^+$	3.04×10^{-25}	8.33×10^{-8}	1.82×10^{-19}
3.347[a]	131	$\frac{7}{2}^+$	1.23×10^{-12}	2.74×10^{-7}	9.84×10^{-7}
3.643[a]	427	$\frac{9}{2}^+$	1.58×10^{-10}	6.09×10^{-9}	1.54×10^{-4}
3.752[a]	536	$\frac{3}{2}^-$	9.94×10^{-5}	1.0×10^{-7}	0.04×10^{-2}
3.901[a]	685	$\frac{7}{2}^-$	8.72×10^{-7}	1.0×10^{-7}	0.07×10^{-2}
4.005[b]	780	$\frac{3}{2}^+$	8.4×10^{-3}	4.39×10^{-7}	0.18×10^{-1}
4.228[b]	1002	$\frac{5}{2}^+$	4.5×10^{-3}	1.0×10^{-6}	0.60
4.539[b]	1313	$\frac{3}{2}^+$	6.5×10^{-2}	1.0×10^{-6}	0.40

[a]The work of Kubono *et al*. assumes a proton threshold of 3.216 MeV.
[b]Excitation energies for states observed in this work assume the proton threshold has the currently accepted value of 3.226 MeV [4].

the ^{15}O(α,γ)^{19}Ne(p,γ)^{20}Na(p,γ)^{21}Mg series of reactions. A study of the ^{15}O(α,γ)^{19}Ne reaction [18] resulted in a limit being set for this rate that was significantly lower than the β-decay rate. When included in hydrodynamic simulations of ONe novae, this suggests breakout along this path is unlikely to occur at novae temperatures.

In attempting to extend these studies to more extreme situations, one faces several challenges: there is additional complexity in the treatment of the hydrodynamics, the hotter and denser environments suggest many more nuclei and reactions are involved, and of course the reaction rates must be known over a higher temperature range. The complex interplay of nuclear reactions that occurs means that reliable estimates of nucleosynthesis and energy production can only be obtained through fully networked hydrodynamic simulations with accurate reaction rates used wherever possible. The first attempts to do this are only now being made [19]. One of the reaction rates to be included is that of ^{20}Na(p,γ)^{21}Mg.

For well-isolated narrow resonances, the average stellar reaction rate per particle pair $\langle\sigma v\rangle$ can be calculated as

$$\langle\sigma v\rangle = \left(\frac{2\pi}{\mu kT}\right)^{3/2} \hbar^2(\omega\gamma)\exp\left(-\frac{E_R}{kT}\right), \qquad (1)$$

where μ is the reduced mass, k is Boltzmann's constant, T is the temperature, and $\omega\gamma$ is the resonance strength given in this case by

$$\omega\gamma = \frac{2J+1}{(2J_{^{20}\mathrm{Na}}+1)(2J_p+1)}\frac{\Gamma_p\Gamma_\gamma}{\Gamma_{\mathrm{tot}}}, \qquad (2)$$

in which J is the spin of the state populated in ^{21}Mg. At these energies, the total width Γ_{tot} can be taken as the sum of the proton and γ-ray partial widths Γ_p and Γ_γ, respectively.

Parameters for each of the contributing states are taken either from the present work or from the work of Kubono *et al*. [3] and are summarized in Table III. The γ widths for the six lowest energy states originate from lifetimes of (tentatively assigned) mirror isobar states in ^{21}F [2], while the γ widths for the two highest energy states have been set at 1eV, a likely upper limit.

In addition to the resonant processes, nonresonant direct capture can also occur. Similarly, the tails of distant resonances will also contribute to the cross section. These effects are small and have been treated with the same formalism used by previous authors [3,20]. To allow easy comparison with the results of Kubono *et al*. [3], we follow their lead in evaluating the reaction rate in an environment of hydrogen density $X_H\rho = 5 \times 10^5$ g/cm^3, typical of novae. Figure 9 shows the contributions of each of the relevant resonances known to exist in ^{21}Mg, the contribution of direct capture, and the total taken as the linear sum of the contributions.

Overall, the inclusion of the new data set has made very little difference to the net reaction rate as previously calculated by Kubono *et al*. The alteration to the resonance energy and spin of the state now located at $E_x(^{21}\mathrm{Mg}) = 4.005$ MeV has somewhat increased this contribution. The states at 4.228 and 4.539 MeV, not included before, also have very little effect except at the highest temperatures where the direct capture contribution also becomes large. Their small contribution stems from the dominance of the γ-decay width in determination of the

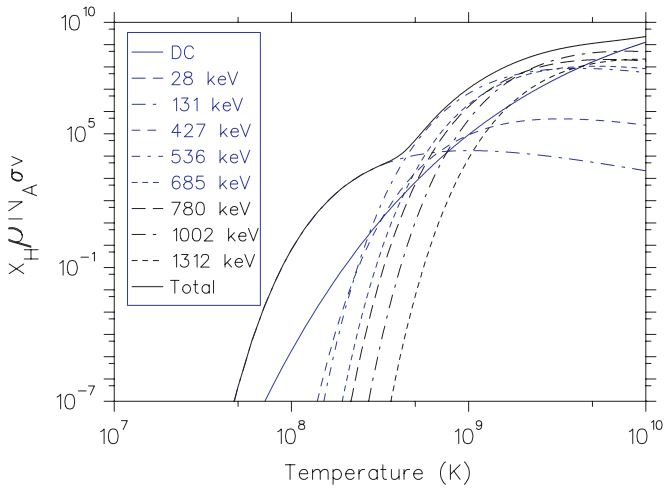

FIG. 9. (Color online) Contributions of various states in ^{21}Mg to the ^{20}Na(p,γ)^{21}Mg reaction rate, together with the total reaction rate calculated as the linear sum of contributions.

reaction rate, and thus a direct measurement of these widths should be conducted: the accurate knowledge of the location of these states provided in this work should aid in this endeavor.

The final aspect that might yet alter the conclusions on the ^{20}Na(p,γ)^{21}Mg reaction rate are the states predicted by the shell model at slightly lower energies than were able to be measured here. The agreement between shell model and observation as demonstrated in this work is impressive, and so the inclusion of the effect of these additional states should be seriously considered. States that could be populated by s-wave proton capture are predicted at $E_x(^{21}\mathrm{Mg}) = 3.512$ MeV ($E_r = 286$ keV) and $E_x(^{21}\mathrm{Mg}) = 3.681$ MeV ($E_r = 455$ keV). Potential candidate states have been observed in the work of Kubono *et al.*, but tentative alternative spin assignments were made. A remeasurement of this region of excitation is suggested.

VI. SUMMARY

The technique of resonant elastic scattering has been used to identify three states in ^{21}Mg. R-matrix analysis, together with comparisons to known analog states, reveals all three to be of s-wave character, to be located at excitation energies of 4.005, 4.228, and 4.539 MeV, and to have proton decay widths of 8, 5, and 65 keV, respectively. Excellent agreement with shell model calculation has allowed unambiguous spin assignments to be made, giving the states $J^\pi = \frac{3}{2}^+$, $\frac{5}{2}^+$, and $\frac{3}{2}^+$, in order of ascending energy. Inclusion of these new data has little net effect on the ^{20}Na(p,γ)^{21}Mg reaction rate, even at higher temperatures. Consequently, this work reinforces the view that breakout from the hot-CNO cycles to the rp-process in novae and x-ray bursts does not proceed through the reaction sequence ^{15}O(α, γ)^{19}Ne(p,γ)^{20}Na(p,γ)^{21}Mg.

ACKNOWLEDGMENTS

The authors thank the operators of the ISAC facility for making these measurements possible. Additionally, we especially thank Dave Hutcheon at TRIUMF for assisting with the measurements performed on the DRAGON spectrometer, and Paul Demaret at the CRC for making the polyethylene targets used in these measurements. The authors acknowledge support from the Engineering and Physical Sciences Research Council (U.K.), the Natural Sciences Research Council of Canada, and the National Science Foundation (U.S.) Grant No. PHY-0244453.

[1] P. von Neumann-Cosel, R. Jahn, U. Fister, T. K. Trelle, and B. A. Brown, Phys. Rev. C **56**, 547 (1997).
[2] D. E. Alburger, C. J. Lister, J. W. Olness, and D. J. Millener, Phys. Rev. C **23**, 2217 (1981).
[3] S. Kubono *et al.*, Nucl. Phys. **A537**, 153 (1992).
[4] R. B. Firestone, Nucl. Data Sheets **103**, 269 (2004).
[5] C. Ruiz, F. Sarazin, L. Buchmann, T. Davinson, R. E. Azuma, A. A. Chen, B. Fulton, D. Groombridge, L. Ling, A. Murphy, J. Pearson, I. Roberts, A. Robinson, A. C. Shotter, P. Walden, and P. J. Woods, Phys. Rev. C **65**, 042801(R) (2002).
[6] C. Ruiz *et al.*, Phys. Rev. C **71**, 025802 (2005).
[7] R. E. Laxdal, Nucl. Instrum. Methods B **204**, 400 (2003).
[8] D. A. Hutcheon *et al.*, Nucl. Phys. **A718**, 515 (2003).
[9] T. Davinson *et al.*, Nucl. Instrum. Methods A **454**, 350 (2000).
[10] D. J. Skyrme, Nucl. Instrum. Methods **57**, 61 (1967).
[11] C. Ruiz, Ph.D. thesis, University of Edinburgh, 2003 (unpublished).
[12] R. G. Thomas, Phys. Rev. **88**, 1109 (1952).
[13] A. M. Lane and R. G. Thomas, Rev. Mod. Phys. **30**, 257 (1958).
[14] F. C. Barker, Aust. J. Phys. **25**, 341 (1972).
[15] B. A. Brown, A. Etchegoyen, N. S. Godwin, W. D. M. Rae, W. A. Richter, W. E. Ormand, E. K. Warburton, J. S. Winfield, L. Zhao, and C. H. Zimmerman, OXBASH for Windows, MSU-NSCL Report Number 1289 (2004).
[16] B. A. Brown and B. H. Wildenthal, Annu. Rev. Nucl. Part. Sci. **38**, 29 (1988).
[17] R. K. Wallace and S. E. Woosley, Astrophys. J. **45** (Suppl.) 389 (1981).
[18] B. Davids, A. M. van den Berg, P. Dendooven, F. Fleurot, M. Hunyadi, M. A. de Huu, R. H. Siemssen, H. W. Wilschut, H. J. Wörtche, M. Hernanz, J. José, K. E. Rehm, A. H. Wuosmaa, and R. E. Segel, Phys. Rev. C **67**, 065808 (2003).
[19] J. José, private communication.
[20] M. Wiescher, J. Görres, F.-K. Thielemann, and H. Ritter, Astron. Astrophys. **160**, 56 (1986).